

A binary main-belt comet

Jessica Agarwal¹, David Jewitt^{2,3}, Max Mutchler⁴, Harold Weaver⁵ & Stephen Larson⁶

Asteroids are primitive Solar System bodies that evolve both collisionally and through disruptions arising from rapid rotation¹. These processes can lead to the formation of binary asteroids^{2–4} and to the release of dust⁵, both directly and, in some cases, through uncovering frozen volatiles. In a subset of the asteroids called main-belt comets, the sublimation of excavated volatiles causes transient comet-like activity^{6–8}. Torques exerted by sublimation measurably influence the spin rates of active comets⁹ and might lead to the splitting of bilobate comet nuclei¹⁰. The kilometre-sized main-belt asteroid 288P (300163) showed activity for several months around its perihelion 2011 (ref. 11), suspected to be sustained by the sublimation of water ice¹² and supported by rapid rotation¹³, while at least one component rotates slowly with a period of 16 hours (ref. 14). The object 288P is part of a young family of at least 11 asteroids that formed from a precursor about 10 kilometres in diameter during a shattering collision 7.5 million years ago¹⁵. Here we report that 288P is a binary main-belt comet. It is different from the known asteroid binaries in its combination of wide separation, near-equal component size, high eccentricity and comet-like activity. The observations also provide strong support for sublimation as the driver of activity in 288P and show that sublimation torques may play an important part in binary orbit evolution.

Hubble Space Telescope (HST) images from December 2011 revealed that 288P could be a binary system at the limits of resolution¹³. Shortly before the next perihelion passage (2016 November 08, at 2.45 astronomical units (AU) from the Sun), 288P passed close to Earth (2016 September 11, at 1.45 AU). The proximity to the Earth made it possible to observe 288P with the HST at a spatial resolution sufficient to clearly resolve the two components of the binary (Fig. 1 and Extended Data Table 1). The components of 288P lie close to the heliocentric orbital plane (Extended Data Fig. 1). The mass of the system, derived from Kepler's third law, is in the range $1.3 \times 10^{12} \text{ kg} < M < 1.1 \times 10^{13} \text{ kg}$, but we cannot meaningfully constrain the density, owing to the unknown dimensions of the components (see Methods).

The two components are similar in their average brightness (Extended Data Table 2), indicating that they are of similar size. At the resolution of the data, we cannot determine which component is the source of the dust, or whether both might be. With no means of distinguishing the two nuclei in the images, we instead base our orbit analysis only on the time-dependence of their apparent separation. We searched a wide parameter space for binary orbit solutions that reproduce the measured component separations (Fig. 2; see also Methods and Extended Data Fig. 2). Orbits that have small eccentricities do not fit the data. The only acceptable solutions have eccentricities $e > 0.6$ and fall into three distinct groups characterized by orbital periods near 103 days, 135 days and 175 days, respectively. These groups all have ratios of the orbital semimajor axis to the primary object radius of about 100, much larger than the ratios (< 10) found in most asteroid binaries (Fig. 3). Although binary asteroids are common¹⁶, 288P is the first to show a wide separation, high eccentricity, similarly sized components and mass-loss activity, suggestive of a different origin.

The HST observations show that 288P reactivated not later than July 2016. Repeated activity near perihelion is a strong indicator of the sublimation of water ice due to increased solar heating. A model of the motion of the dust under the influence of solar gravity and radiation pressure suggests that the activity began with a brief release of comparatively large (millimetre-sized) grains in July, whereas from mid-September until at least the end of January 2017 (the last of our observations), the dominant grain size fell to about $10 \mu\text{m}$ (Extended Data Fig. 3). This indicates that the developing gas production first lifted a layer of large, loosely connected grains, possibly deposited around the end of the previous period of activity in 2011/12 (ref. 17). After their removal and with decreasing heliocentric distance, the gas drag became strong enough to lift smaller particles as well. The dust production rates were of the order of $0.04\text{--}0.1 \text{ kg s}^{-1}$ (see Methods and Extended Data Fig. 4), in contrast to 1 kg s^{-1} inferred from 2011 data¹³.

The majority of small binary asteroid systems (Fig. 3) probably formed by rotational fission^{2–4} and subsequently evolved under the action of tides and weak radiation torques. The post-formation evolution depends on the relative sizes of the components, their shapes and spins, and their thermal and mechanical properties⁴. In binaries with unequal components (size ratio < 0.6 , called group A in Fig. 3), the larger (primary) body retains the fast spin rate of the precursor, and only the secondary can be synchronized with the binary orbit¹⁸. In binaries with a larger size ratio (group B), the component spin rates and binary orbital period can be synchronized by mutual tides. Binary systems created directly from the rotational fission of a strengthless precursor body can have semimajor axes of up to $34R_p$, where R_p is the radius of the primary¹⁸. The 288P system has a semimajor axis of at least $76R_p$ and so cannot have formed directly from rotational fission of a strengthless precursor. The semimajor axis of a tidally locked binary system can, however, be expanded beyond the $34R_p$ limit through the action of radiative torques (the binary YORP effect)¹⁹. At least in systems with a low size ratio (group A), this can lead to the formation of wide asynchronous binaries (group W), which remain stable after the secondary spin and orbital period decouple²⁰.

Wide binaries might also form in the aftermath of a catastrophic impact generating fragments of similar size that subsequently enter into orbit about each other²¹. It is possible that the event forming the (7.5 ± 0.3) -million-year-old 288P family¹⁵ created such an escaping ejecta binary (EEB). EEBs contain $< 10\%$ of the total mass involved in a catastrophic collision^{21,22}, such that they are less numerous than single fragments susceptible to rotational splitting. If formed as an EEB, the activity of 288P might have been triggered by a more recent sub-catastrophic impact or rotational mass-shedding following YORP spin-up of one of the components not causally related to the binary formation. The average time interval between impacts of the relevant size is 10^5 years (see Methods), and the nominal YORP spin-up timescale of a 1-km asteroid is $10^5\text{--}10^6$ years (ref. 18), but with considerable uncertainty because the YORP effect depends sensitively on a body's shape and material properties. Hence, both impact activation and YORP-driven rotational fission are plausible in the time since the family-forming collision. The high eccentricity of the system is consistent with both the EEB and

¹Max Planck Institute for Solar System Research, Justus-von-Liebig Weg 3, 37077 Göttingen, Germany. ²Department of Earth, Planetary and Space Sciences, University of California at Los Angeles, 595 Charles Young Drive East, Los Angeles, California 90095-1567, USA. ³Department of Physics and Astronomy, University of California at Los Angeles, 430 Portola Plaza, Box 951547, Los Angeles, California 90095-1547, USA. ⁴Space Telescope Science Institute, 3700 San Martin Drive, Baltimore, Maryland 21218, USA. ⁵The Johns Hopkins University Applied Physics Laboratory, 11100 Johns Hopkins Road, Laurel, Maryland 20723, USA. ⁶Lunar and Planetary Laboratory, University of Arizona, 1629 East University Boulevard, Tucson, Arizona 85721-0092, USA.

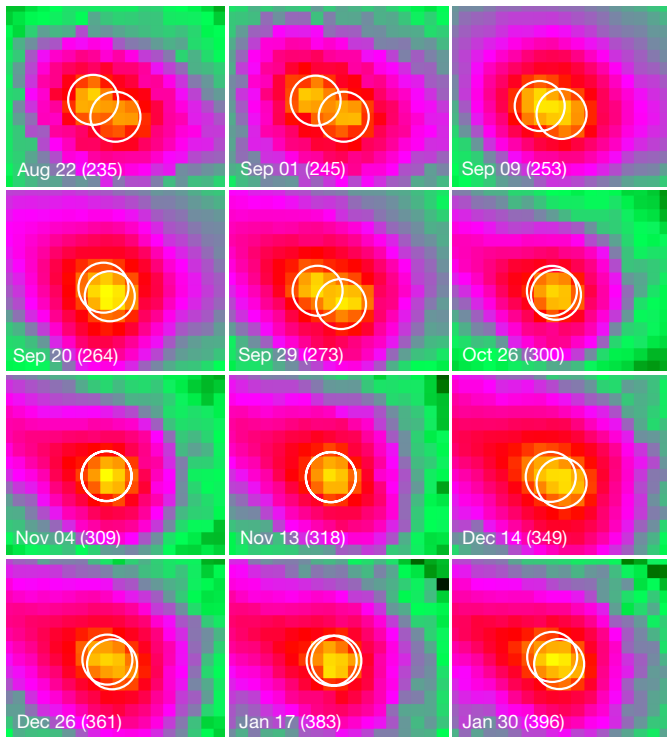


Figure 1 | The 288P system between August 2016 and January 2017.

The images were obtained with the $1\text{k} \times 1\text{k}$ CIK1C subarray of the Wide Field Camera 3 of the HST and the wide passband filter F606W, centred at 595.6 nm. Details of the observations are listed in Extended Data Table 1. Each panel is a composite of eight single exposures of 230 s, obtained with a 2×2 subsampling dither-pattern that enabled us to re-sample the images to a pixel scale of $0.025''$. Each panel is $0.45'' \times 0.38''$ in size. The intensity scale is logarithmic, and the range was adjusted manually for each image to account for the changing brightness. The appearance of 288P alternated between two clearly separated nuclei of similar brightness and a single point source, confirming that 288P is a binary asteroid. We measured the distance by visually fitting circles of radius two pixels to the point spread functions of the two components. We estimate the 3-sigma uncertainty of the measured distance between their centres to be ± 0.5 pixel ($\pm 0.013''$). The numbers in parentheses indicate the day of the year, starting from 2016 January 01.

the rotational fission scenario, as tidal damping of the eccentricity occurs on timescales longer than the age of the 288P family²⁰.

The YORP torque influences the obliquity^{23–25}, driving about 50% of the objects to obliquities of 0° or 180° (ref. 26). Therefore, the mutual orbit of a binary system formed by rotational fission has an elevated probability of being aligned with the heliocentric orbit, as is observed in 288P (see Extended Data Fig. 1). If 288P were an EEB, the alignment of the binary and heliocentric orbits would have to be considered a coincidence for which the statistical probability is around 1% (see Extended Data Fig. 1). Given this low probability and the low mass fraction of EEBs indicated by collision models, rotational fission seems the more likely formation process of 288P.

Surface ice cannot survive in the asteroid belt for the age of the Solar System but can be protected for billion-year timescales by a refractory dust mantle only a few metres thick²⁷. It is therefore likely that an event splitting a body into two parts of similar size will uncover buried ice if present. A decisive factor for the subsequent development of the system is whether the sublimation will last longer than the time required to tidally synchronize the spin and binary orbital periods, which is 5,000 years for equal-mass components but orders of magnitude longer for lower mass ratios²⁰. Sublimation-driven activity can last longer than 5,000 years²⁸, such that for high-mass ratio systems it is conceivable that activity prevails after tidal synchronization. In this case, the recoil force from the local sublimation of water ice can drive binary evolution. Subject to the many unknowns, we find that the timescale to

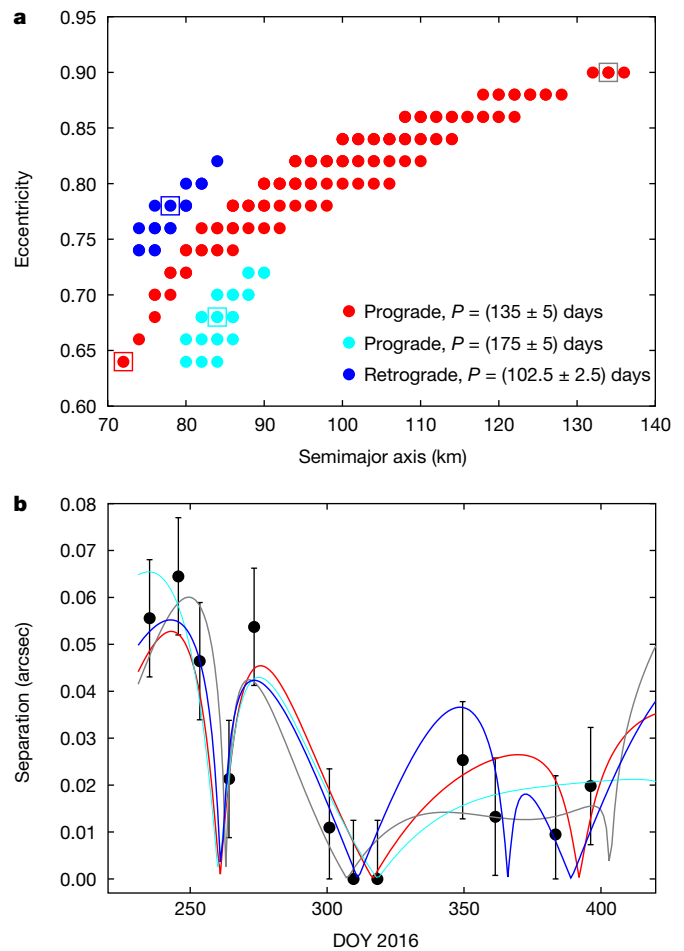


Figure 2 | Binary orbits matching the observations. To infer the Keplerian elements of the mutual orbit, we calculated the projected distances at the times of the observations for a large set of both prograde and retrograde orbits, varying five parameters independently: the semimajor axis, a , between 40 and 150 km in steps of 2 km, the eccentricity, e , between 0 and 0.98 in steps of 0.02, the orbital period, P , between 20 and 210 days in steps of 5 days, the time of perihelion in steps of $1/20$ of the orbital period, and the angle, α_0 , between the perihelion vector and the line of sight on 2016 August 22 in steps of 10° . To account for the changing observing geometry, we subtracted the difference in geocentric ecliptic longitude between August 22 and the date of observation from α_0 for each observation date (see Methods and Extended Data Fig. 2). We searched this parameter space for combinations reproducing all 12 measurements. **a**, The acceptable combinations of the semimajor axis a and eccentricity e . Red and light blue symbols refer to prograde orbits with ($130 < P < 140$) days and ($170 < P < 180$) days, respectively, whereas dark blue symbols represent retrograde orbits with ($100 < P < 105$) days. All solutions have the line of sight on August 22 within $\pm 10^\circ$ of the system's major axis, and a periapsis date between September 16 and September 21. **b**, The measured and simulated component distance for four representative orbit solutions marked by boxes of the same colour in the upper panel. These four solutions were chosen to reflect the diversity of the possible orbits. The error bars of $\pm 0.013''$ reflect the estimated 3-sigma position uncertainty of the circles in Fig. 1. The measured component distances are listed in Extended Data Table 2. DOY, day of year, starting from 2016 January 1.

change the orbit of a synchronous binary system by sublimation torques can be several orders of magnitude shorter than for radiation torques (see Methods). For this reason, it seems more likely that 288P's wide separation reflects the action of sublimation torques, although binary YORP and subsequent reactivation cannot be excluded. The evolutionary paths discussed here are illustrated in Extended Data Fig. 5.

Most asteroid binaries are discovered either by radar, when close to the Earth, or by mutual eclipses in their light curves, when the

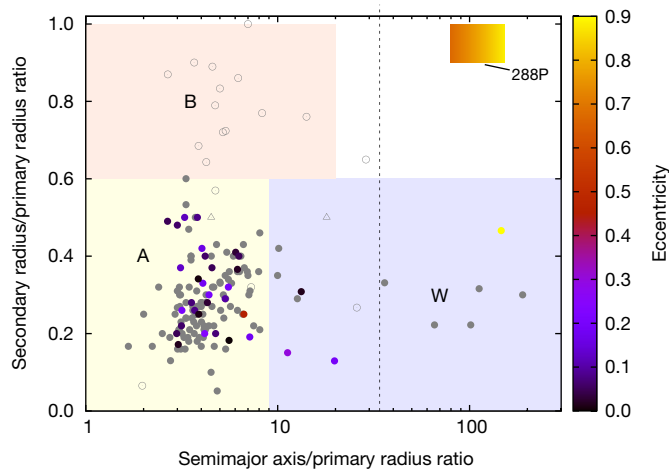


Figure 3 | Orbital properties of 288P and of previously known binary asteroids. The plot shows the size ratio as a function of the ratio of semimajor axis to primary radius for all asteroids with known primary and secondary radius and semimajor axis²⁹. The eccentricity is colour-coded, with grey symbols used for systems with unmeasured eccentricity. Filled circles represent systems with a primary rotation period $P < 5$ h, open circles $P > 5$ h, and triangles an unknown primary rotation period. The dotted line corresponds to $34R_p$, the upper limit for binaries to form directly from a strengthless precursor¹⁸. The letters A, B and W and the colour shading reflect the three main groups of known small asteroid binaries². Group A binaries have a size ratio < 0.6 and a fast-rotating primary and, in two-thirds of the systems, a secondary rotating synchronously with the binary orbit. Group B consists of doubly synchronous systems with similar component size. Group W consists of wide, asynchronous binaries. All three groups are consistent with an origin by rotational fission¹⁸. The effect of tides on the spin state depends on the component size ratio and distinguishes groups A and B. Group W possibly evolved out of group A under the action of the binary YORP effect²⁰. The object 288P occupies a region in this parameter space that has until now been unpopulated. We estimate a lower limit of 0.8 for its cross-section ratio from the maximum brightness difference (0.2 mag) of the two components in individual exposures. This corresponds to a radius ratio of 0.9. The combined double-peaked light curve of 288P shows a 16-h periodicity¹⁴. This constrains the more variable component to a 16-h rotation period, whereas the rotation of the second component, if less variable, is not well constrained by the light curve.

component separations are small. Kilometre-sized asteroids in the main belt are too small and distant to be studied by radar, and wide binaries align to produce mutual eclipses only rarely. As a result, there is a strong observational bias against the detection of small, wide, main-belt binaries of the sort exemplified by 288P. The binary nature of 288P was discovered as a by-product of the activity of this body, which attracted attention and motivated the initial HST observations. Although there are many biases against the detection of wide binaries in the asteroid belt, there is no obvious bias against detecting systems with similar component sizes. Still, the previously known six wide binaries have a diameter ratio of about 0.3 (Fig. 3), whereas in 288P this ratio is close to unity. This suggests that 288P is of a rare type even beyond the detection bias. A larger sample of wide binaries is needed to establish whether high-mass ratio systems are more likely to be active than low-mass ratio systems. Based on currently available models, the most probable formation scenario of 288P is rotational break-up followed by rapid synchronization and orbit extension by sublimation torques. This path would be much less probable in low-mass ratio systems because of the longer synchronization timescale. It is therefore possible that the activity played a decisive role in the formation of the 288P system, and that the high mass ratio was a prerequisite for that.

Online Content Methods, along with any additional Extended Data display items and Source Data, are available in the online version of the paper; references unique to these sections appear only in the online paper.

Received 2 May; accepted 25 July 2017.

- Marzari, F., Rossi, A. & Scheeres, D. J. Combined effect of YORP and collisions on the rotation rate of small main belt asteroids. *Icarus* **214**, 622–631 (2011).
- Pravec, P. & Harris, A. W. Binary asteroid population. 1. Angular momentum content. *Icarus* **190**, 250–259 (2007).
- Walsh, K. J., Richardson, D. C. & Michel, P. Rotational breakup as the origin of small binary asteroids. *Nature* **454**, 188–191 (2008).
- Walsh, K. J. & Jacobson, S. A. in *Asteroids IV* (eds Michel, P. et al.) 375–393 (Univ. Arizona Press, 2015).
- Jewitt, D. et al. Anatomy of an asteroid breakup: the case of P/2013 R3. *Astron. J.* **153**, 223 (2017).
- Hsieh, H. H. & Jewitt, D. A population of comets in the main asteroid belt. *Science* **312**, 561–563 (2006).
- Jewitt, D. The active asteroids. *Astron. J.* **143**, 66 (2012).
- Jewitt, D., Hsieh, H. & Agarwal, J. in *Asteroids IV* (eds Michel, P. et al.) 221–241 (Univ. Arizona Press, 2015).
- Keller, H. U., Mottola, S., Skorov, Y. & Jorda, L. The changing rotation period of comet 67P/Churyumov–Gerasimenko controlled by its activity. *Astron. Astrophys.* **579**, L5 (2015).
- Hirabayashi, M. et al. Fission and reconfiguration of bilobate comets as revealed by 67P/Churyumov–Gerasimenko. *Nature* **534**, 352–355 (2016).
- Hsieh, H. H. et al. Discovery of main-belt comet P/2006 VW₁₃₉ by Pan-STARRS1. *Astrophys. J.* **748**, L15 (2012).
- Licandro, J. et al. Exploring the nature of new main-belt comets with the 10.4 m GTC telescope: (300163) 2006 VW₁₃₉. *Astron. Astrophys.* **550**, A17 (2013).
- Agarwal, J., Jewitt, D., Weaver, H., Mutchler, M. & Larson, S. Hubble and Keck telescope observations of active asteroid 288P/300163 (2006 VW₁₃₉). *Astron. J.* **151**, 12 (2016).
- Waniak, W. & Drahus, M. Gemini and Keck observations of slowly rotating, bilobate active asteroid (300163). In *AAS/Division for Planetary Sciences Meeting Abstracts Vol. 48*, 504.01 (2016).
- Novaković, B., Hsieh, H. H. & Cellino, A. P/2006 VW₁₃₉: a main-belt comet born in an asteroid collision? *Mon. Not. R. Astron. Soc.* **424**, 1432–1441 (2012).
- Margot, J.-L., Pravec, P., Taylor, P., Carry, B. & Jacobson, S. in *Asteroids IV* (eds Michel, P. et al.) 355–374 (Univ. Arizona Press, 2015).
- Rotundi, A. et al. Dust measurements in the coma of comet 67P/Churyumov–Gerasimenko inbound to the Sun. *Science* **347**, aaa3905 (2015).
- Jacobson, S. A. & Scheeres, D. J. Dynamics of rotationally fissioned asteroids: source of observed small asteroid systems. *Icarus* **214**, 161–178 (2011).
- Čuk, M. & Burns, J. A. Effects of thermal radiation on the dynamics of binary NEAs. *Icarus* **176**, 418–431 (2005).
- Jacobson, S. A., Scheeres, D. J. & McMahon, J. Formation of the wide asynchronous binary asteroid population. *Astrophys. J.* **780**, 60 (2014).
- Durda, D. D. et al. The formation of asteroid satellites in large impacts: results from numerical simulations. *Icarus* **167**, 382–396 (2004).
- Durda, D. D. The formation of asteroidal satellites in catastrophic collisions. *Icarus* **120**, 212–219 (1996).
- Vokrouhlický, D., Nesvorný, D. & Bottke, W. F. The vector alignments of asteroid spins by thermal torques. *Nature* **425**, 147–151 (2003).
- Hanuš, J. et al. A study of asteroid pole-latitude distribution based on an extended set of shape models derived by the lightcurve inversion method. *Astron. Astrophys.* **530**, A134 (2011).
- Cibulková, H., Durech, J., Vokrouhlický, D., Kaasalainen, M. & Oszkiewicz, D. A. Distribution of spin-axis longitudes and shape elongations of main-belt asteroids. *Astron. Astrophys.* **596**, A57 (2016).
- Vokrouhlický, D. & Čapek, D. YORP-induced long-term evolution of the spin state of small asteroids and meteoroids: Rubincam's approximation. *Icarus* **159**, 449–467 (2002).
- Schorghofer, N. The lifetime of ice on main belt asteroids. *Astrophys. J.* **682**, 697–705 (2008).
- Capria, M. T., Marchi, S., de Sanctis, M. C., Coradini, A. & Ammannito, W. The activity of main belt comets. *Astron. Astrophys.* **537**, A71 (2012).
- Johnston, W. R. Binary minor planets V9.0. *NASA Planetary Data System* 244 (2016).

Acknowledgements This work is based on observations made with the NASA/ESA HST, obtained at the Space Telescope Science Institute, which is operated by the Association of Universities for Research in Astronomy, Inc., under NASA contract NAS 5-26555. These observations are associated with programmes 12597, 14790, 14864 and 14884.

Author Contributions J.A. identified the potential binary nature of 288P, applied for HST observing time, carried out the model calculations regarding the binary orbit and the dust dynamics, and led the manuscript preparation. D.J. calculated the importance of the sublimation-driven torque and contributed to the interpretation and presentation of the data. M.M. processed the raw images and was responsible for the removal of cosmic rays and the production of the sub-sampled composite images. H.W. contributed to designing and preparing the observations. S.L. checked the work and critiqued the proposals and paper.

Author Information Reprints and permissions information is available at www.nature.com/reprints. The authors declare no competing financial interests. Readers are welcome to comment on the online version of the paper. Publisher's note: Springer Nature remains neutral with regard to jurisdictional claims in published maps and institutional affiliations. Correspondence and requests for materials should be addressed to J.A. (agarwal@mps.mpg.de).

Reviewer Information *Nature* thanks D. Bodewits and D. Scheeres for their contribution to the peer review of this work.

METHODS

Orbit calculation. The relative motion of two bodies in orbit about their centre of mass can be described by a Keplerian ellipse with one of the bodies fixed at one focus point and the other orbiting it along the periphery according to Kepler's laws. The length of the radius vector of the ellipse corresponds to the objects' mutual distance, and the true anomaly to the angular distance from the common semimajor axis of the system. The eccentricity and period are the same as for the two individual orbits.

The line connecting the two nuclei is in all images consistent with the projected orbit, and the angle between the line of sight from the Earth to 288P and its orbital plane was $<2.3^\circ$ during all observations. We therefore assume for the following model that the observer was always in the orbital plane of the binary system.

Extended Data Fig. 2a shows the relative orbit of the binary system and a line of sight from the Earth, as they would be seen from an ecliptic northern polar position. The apparent physical distance, d , of the components at time t is described by $d(t) = |\sin(\theta_p(t) - \alpha(t))|$, where $\theta_p(t)$ is the true anomaly for a prograde orbit, and $\alpha(t)$ is the angle between the system's semimajor axis and the line of sight. For a retrograde orbit, and keeping the definition of α , the distance is given by $d(t) = |\sin(\theta_r(t) + \alpha(t))|$.

The angle α changes with time owing to the relative motion of the Earth and the binary system. Extended Data Fig. 2b shows the apparent motion of 288P during the time frame of our observations in the observer-centred ecliptic coordinate system. While the ecliptic longitude varies by 25° , the latitude changes by only 3° . We therefore approximate the change in α by the change in observer-centred ecliptic longitude λ . We define α_0 to be the angle between the line of sight and the system's semimajor axis during the first HST observation on 2016 August 22, and α_0 is a free parameter of our orbit-fitting simulation. The time-dependence of α is then given from the known change in λ , with $\alpha(t) = \alpha_0 + \lambda(t) - \lambda_0$, where λ_0 is the observer-centred ecliptic longitude of 288P on 2016 August 22.

System mass and density. The density is calculated from the total mass, M , and volume, V , of the system. The mass is given by Kepler's law

$$M = \frac{4\pi^2 a^3}{GP^2} \quad (1)$$

where G is the gravitational constant and P is the orbital period, and is found to be in the range $1.3 \times 10^{12} \text{ kg} < M < 1.1 \times 10^{13} \text{ kg}$ for the combinations of a and P compatible with the data (Fig. 2). The total volume, V , of the two nuclei is approximated by that of two spheres having the total cross-section A :

$$V = \sqrt{\frac{8}{9\pi}} A^{3/2} \quad (2)$$

Assuming $A = 5.3 \times 10^6 \text{ m}^2$ (ref. 13), we find $V = 6.5 \times 10^9 \text{ m}^3$. To estimate the uncertainty of the volume, we consider the ratio of the smallest to the largest observed cross-section for one of the components to be 0.7, corresponding to a light-curve amplitude of 0.4 mag (ref. 14). Not knowing the rotational phase at which our observation was made, we estimate that our measured cross-section represents the mean cross-section with an uncertainty of 20%, and that therefore the uncertainty of the volume estimate is 30%. This is a lower limit, because we do not know the extent of the components in the third dimension and the overall shapes of the bodies. To account for these and the (comparatively small) uncertainty of the albedo, we assume a total volume uncertainty of 60%. Combining the smallest (largest) possible mass with the largest (smallest) possible volume, we find densities between 120 kg m^{-3} and $4,200 \text{ kg m}^{-3}$, consistent with typical asteroid densities³⁰ of $1,500 \text{ kg m}^{-3}$.

Dust production. We estimate the dust production rate from the brightness of the coma within a projected aperture of 400 km (corresponding to between 8 and 15 pixels, depending on geocentric distance). For each observation, we measured the flux F_{ap} within circular apertures of increasing radius r_{ap} . The flux rises linearly with r_{ap} , with different slopes for $r_{\text{ap}} < 7 \text{ px}$ and $r_{\text{ap}} > 7 \text{ px}$. Assuming that at $r_{\text{ap}} > 7 \text{ px}$ the surface brightness is dominated by dust, we fit a linear relation $F(r_{\text{ap}}) = F_n + k r_{\text{ap}}$ to $F_{\text{ap}}(r_{\text{ap}})$, where F_n is the nucleus flux and $F_c(r_{\text{ap}}) = k r_{\text{ap}}$ is the flux of light reflected by dust inside the aperture. The uncertainty of the flux measurement is small compared with those of the albedo, phase function, bulk density, size and velocity of the dust used in the following to convert the surface brightness to a production rate.

We convert the measured flux F (in electrons per second) to apparent magnitudes using $m_V = -2.5 \log_{10} F + Z$, where V indicates visual, with $Z = 25.99$ for the F606W filter³¹, and to absolute magnitudes H_V assuming a C-type phase function with $G = 0.15$. Using an S-type phase function with $G = 0.25$ instead would render H_V fainter by 0.14 mag at the largest observed phase angle, reducing the corresponding dust cross-section by 10%.

The total dust cross-section in the aperture is given by $C = 1,329^2 \pi \times 10^{-0.4H_V} / (4p_V)$, where we use a low geometric albedo of $p_V = 0.05$. With $p_V = 0.1$, the dust cross-section would reduce by a factor of 2. The combination of $G = 0.15$ and $p_V = 0.05$ that we used here implies that the derived cross-section is at the lower end of the possible range.

We convert this area to a mass assuming representative particle radii of 6 and 60 μm , respectively, and a bulk density of $1,000 \text{ kg m}^{-3}$, which is also a low value, with typical C-type nucleus densities³⁰ ranging from $1,000$ to $2,000 \text{ kg m}^{-3}$, such that the derived mass represents a lower limit and could be a factor of 4 higher. Additional uncertainty is introduced by our lack of knowledge of whether the density of asteroid dust can be compared to that of the nuclei, and whether dust of the same size dominates the optical cross-section and the mass of the ejected material.

Using the velocity-size relation derived from 2011 HST data¹³, we calculate the dust production rate from the time that a dust particle would remain inside the aperture depending on its size. The statistical uncertainty of the velocity is 30% (from the scatter of the data points in figure 11 of ref. 13). This velocity represents a lower limit because it is only the component perpendicular to the orbital plane, such that the derived production rate is also a lower limit. Extended Data Fig. 5 shows the inferred dust production rates for the two different assumptions of the dominant grain size.

Impact timescale. We estimate the average time interval between impacts excavating the amount of ice required to explain the observed dust production as follows. To explain the dust production rate of 1 kg s^{-1} (ref. 13), and assuming a dust-to-gas mass ratio of 1–10, an ice-sublimating active patch of (30–90) m in radius is required on a perfectly absorbing body at the heliocentric distance of 2.45 AU. A crater of this size on a strengthless rubble pile would have been generated by a 1-m-sized projectile³² impacting at the typical relative velocity of main-belt objects of 5 km s^{-1} (ref. 33). The collisional lifetime (probability of being impacted by a 30-m radius asteroid) of a main-belt asteroid of 1 km radius is 10^9 years (ref. 34). The abundance of 1-m-scale asteroids is uncertain, but they are probably about a factor of 10^4 more numerous than those with 30-m radius³⁴, such that the time interval between impacts of 1-m bodies on a 1-km asteroid is 10^5 years, considerably less than the age of the 288P family. Impact activation is therefore plausible.

Orbital torque by sublimation. Assuming that the dust production was driven by a comparable gas production rate Q_{gas} , and that the gas was leaving the nucleus with the thermal expansion speed of v_{th} from a small patch, this directed emission of gas exerts a torque, T , which could have influenced the binary orbit if the torque was tangential to the orbit, and the orbit and the rotation of the active component were synchronous. The maximum torque is given by

$$T = k Q_{\text{gas}} v_{\text{th}} r \quad (3)$$

where $0 < k < 1$ is a dimensionless parameter describing the degree of collimation of the gas flow (with $k = 0$ corresponding to isotropic ejection and $k = 1$ to perfectly collimated ejection), and r is the radius vector of the binary orbit. Over one mutual orbit of period P , this gives a change in angular momentum of

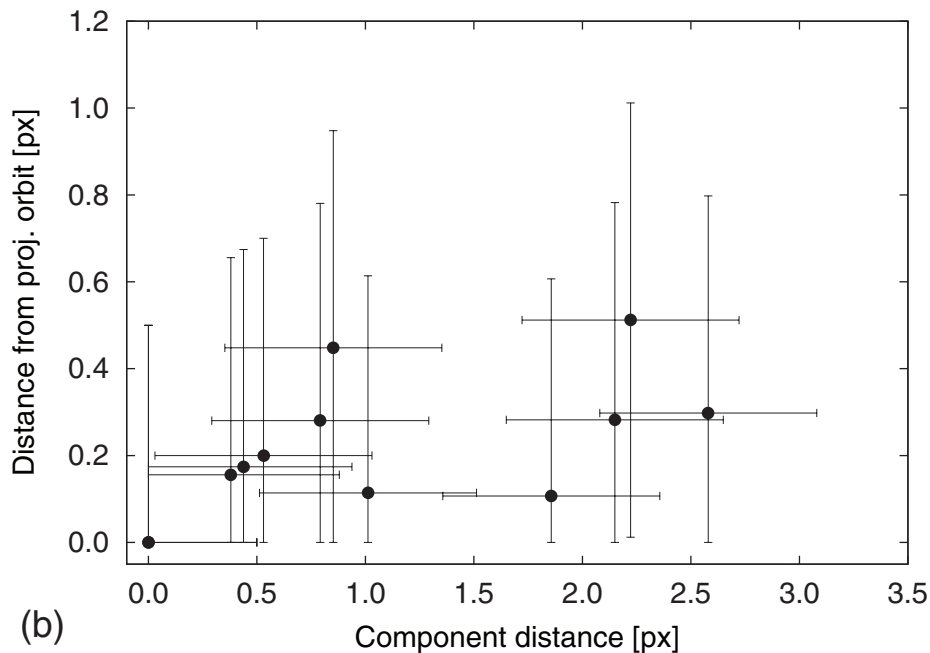
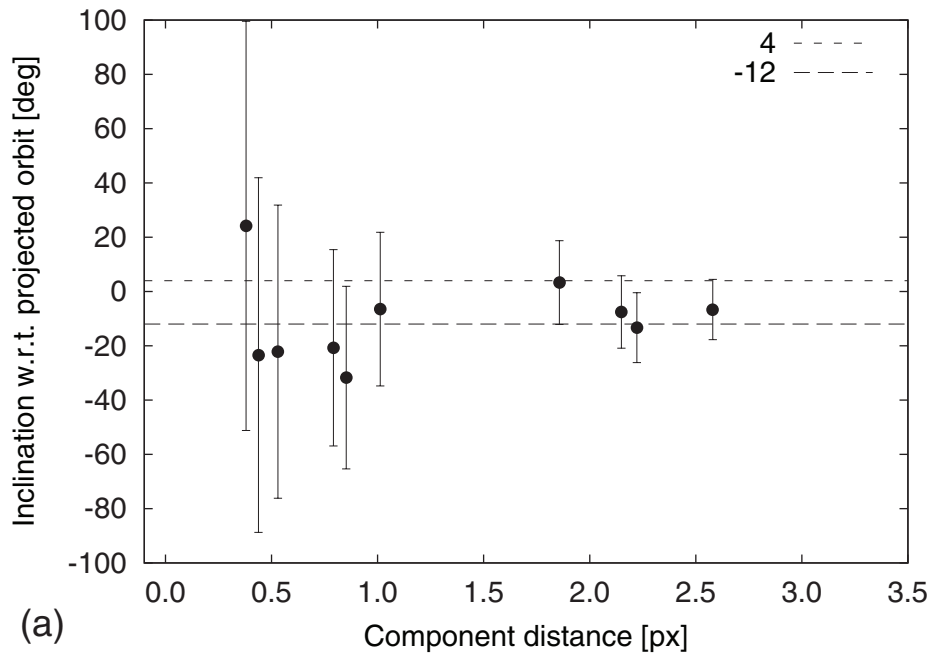
$$\Delta L = k Q_{\text{gas}} v_{\text{th}} \int_0^P r dt \quad (4)$$

We approximate this by $\Delta L = k Q_{\text{gas}} v_{\text{th}} a P$, and assume $k = 0.1$, $v_{\text{th}} = 500 \text{ m s}^{-1}$, $Q_{\text{gas}} = 0.1 \text{ kg s}^{-1}$, an initial $a = 30 \text{ km}$, and $P = 30$ days, obtaining $\Delta L = 4 \times 10^{11} \text{ kg m}^2 \text{ s}^{-1}$. Comparing this to the total angular momentum of the 288P binary orbit (about $5 \times 10^{14} \text{ kg m}^2 \text{ s}^{-1}$), and given that 288P is active for about 10% of each orbit, we find that it would take of order 10^4 revolutions of the binary orbit (about 5×10^3 years) to change the total angular momentum by a factor of 2. We note that both the k -parameter and Q_{gas} influence ΔL linearly, such that the timescale easily has an uncertainty of an order of magnitude or more. Nevertheless, the calculation shows that sublimation torques can change a binary orbit over much shorter timescales than the photon-driven binary YORP effect, which doubles the semimajor axis in $(3\text{--}6) \times 10^4$ years (ref. 20).

Code availability. We have opted not to make the code used to calculate the orbit fit and the synchrony-sydney analysis available because custom routines were developed for this analysis.

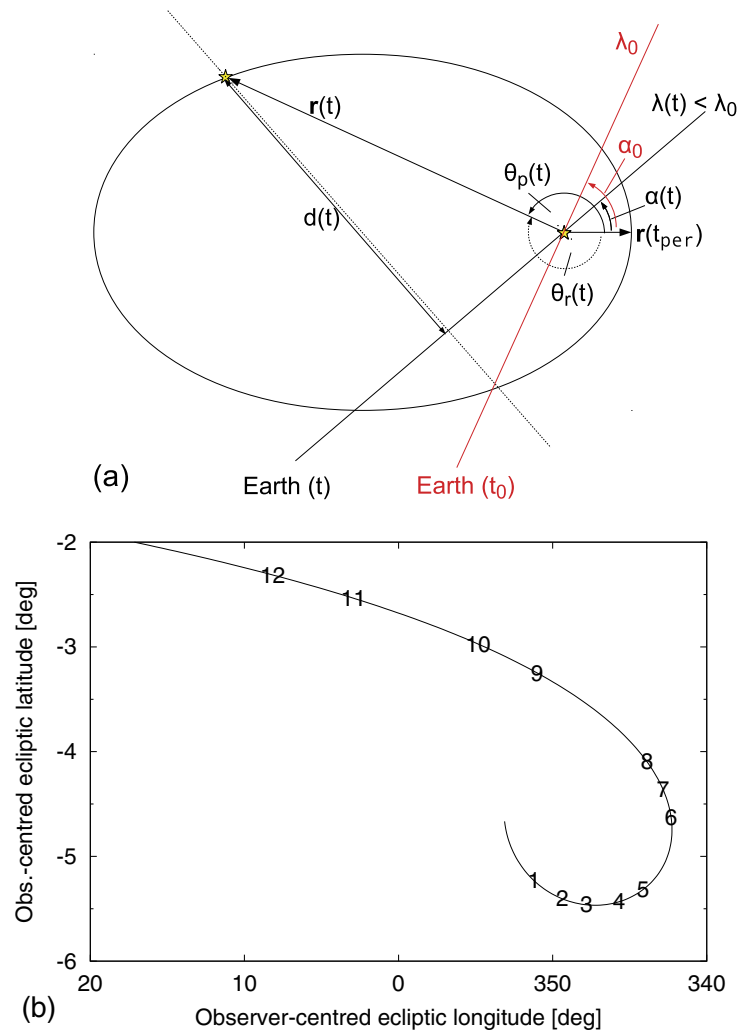
Data availability. The HST data sets analysed during the current study are available in the Mikulski Archive for Space Telescopes (<https://archive.stsci.edu>). The orbital data shown in Fig. 3 are available in the NASA Planetary Data System under identifier EAR-A-COMPIL-5-BINMP-V9.0 (<https://pdsquery.jpl.nasa.gov>). All other data sets generated during the current study are available from the corresponding author on reasonable request.

30. Hanuš, J. *et al.* Volumes and bulk densities of forty asteroids from ADAM shape modeling. *Astron. Astrophys.* **601**, A114 (2017).
31. Kalirai, J. S. *et al.* *WFC3 SMOV Proposal 11450: The Photometric Performance and Calibration of WFC3/UVIS*. Instrument Science Report WFC3 2009-31 (November 2009).
32. Housen, K. R. & Holsapple, K. A. Ejecta from impact craters. *Icarus* **211**, 856–875 (2011).
33. Bottke, W. F., Nolan, M. C., Greenberg, R. & Kolvoord, R. A. Velocity distributions among colliding asteroids. *Icarus* **107**, 255–268 (1994).
34. Bottke, W. F. *et al.* Linking the collisional history of the main asteroid belt to its dynamical excitation and depletion. *Icarus* **179**, 63–94 (2005).
35. Dressel, L. *Wide Field Camera 3 Instrument Handbook for Cycle 25 V9.0* (STScI, 2017).
36. Finson, M. L. & Probstein, R. F. A theory of dust comets. I. Model and equations. *Astrophys. J.* **154**, 327–352 (1968).



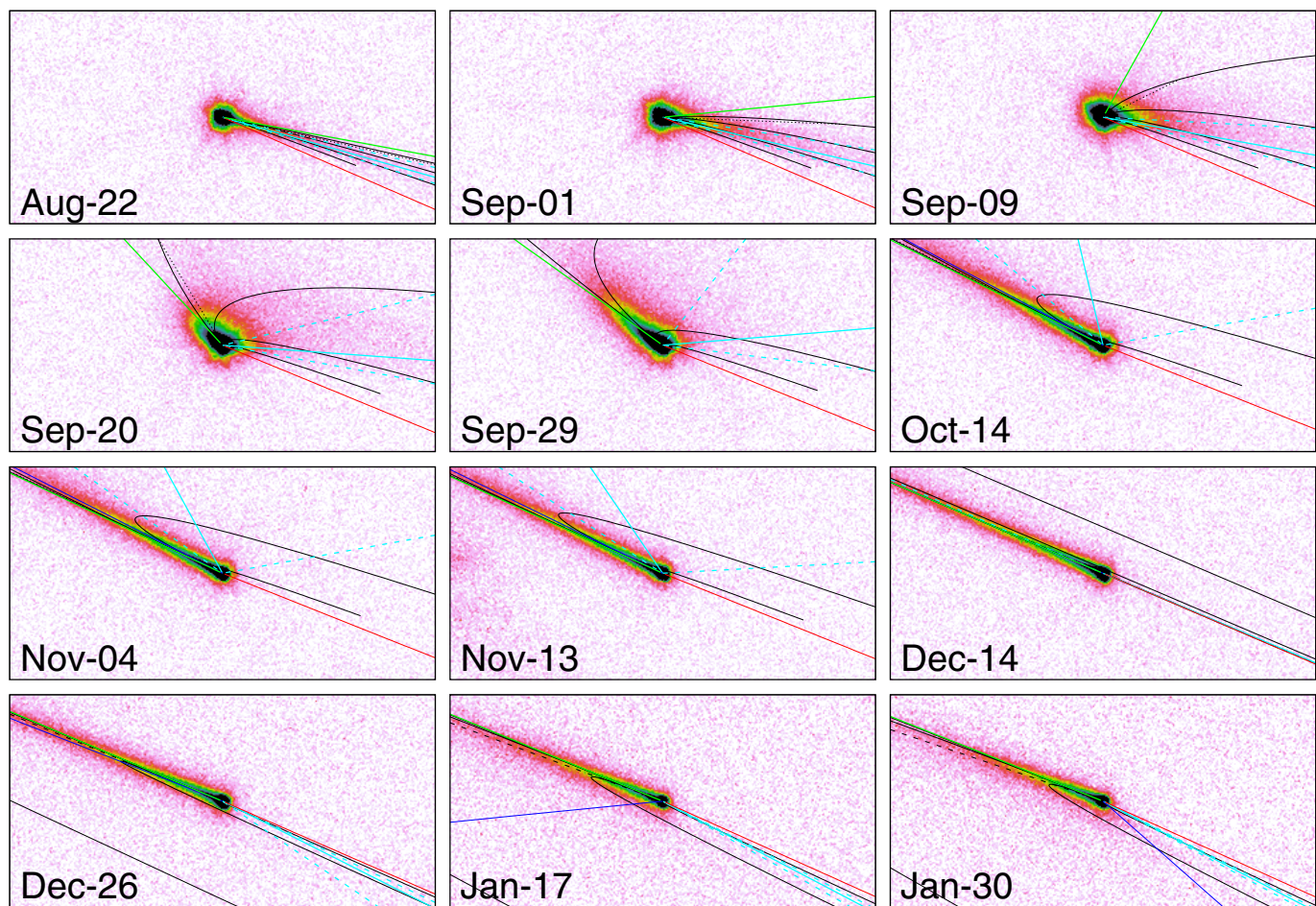
Extended Data Figure 1 | Comparison of the binary orbit to the projected heliocentric orbit. **a.** Difference in on-sky position angle between the line connecting the two components and the projected heliocentric orbit. The measurements at large component distances (>1.5 px) are consistent with projected inclinations between $+4^\circ$ and -12° . The error bars in both panels represent the uncertainty propagated from the position uncertainty in Fig. 1. **b.** Component distance perpendicular to the projected orbit, β . Near conjunction (separation <1.5 px), these measure the angle α between the heliocentric and binary orbit

perpendicular to the image plane through the relation $\sin \alpha = \Delta/D \sin \beta$, where Δ is the geocentric distance and D is the component separation along the line of sight. We assume $D = 100$ km and $\Delta = 2$ au. With $\beta_{\max} = 0.45$ px, we obtain $\alpha_{\max} = 9^\circ$. In conclusion, our best estimate of the binary orbit pole orientation is $(-4 \pm 8)^\circ$ in the image plane and $(0 \pm 9)^\circ$ perpendicular to it, and we describe the uncertainty of the pole direction by a double cone of opening angle 18° . This corresponds to a solid angle of 0.15 sr, or 1% of 4π .



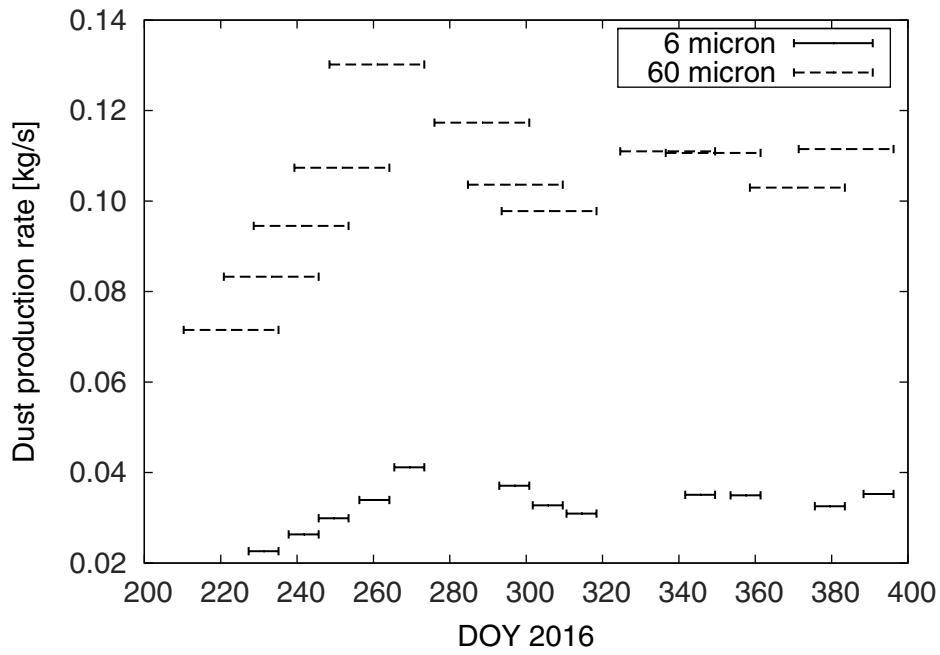
Extended Data Figure 2 | Orbital and observational geometry during the HST observations. **a**, Binary orbit and line of sight from Earth at an arbitrary fixed time t (black) and with respect to the viewing geometry at a specific reference time (red), seen from the north ecliptic pole. The vector $\mathbf{r}(t)$ describes the motion of one component with respect to the other fixed in one focus of the elliptic orbit. t_{per} , time of periastris passage; θ_p, θ_r , true anomaly of a prograde and retrograde orbit; d , projected physical distance

of the components; $\alpha(t)$, angle between the line of sight and the semimajor axis of the system; λ , observer-centered ecliptic longitude; the index 0 refers to the time t_0 (2016 August 22). **b**, Apparent motion of the 288P system to an Earth-based observer in ecliptic longitude and latitude over the timeframe of the HST observations. The coordinates at the times of the 12 observations are indicated by numbers, with 1 corresponding to 2016 August 22, and 12 to 2017 January 30 (see Extended Data Table 1).



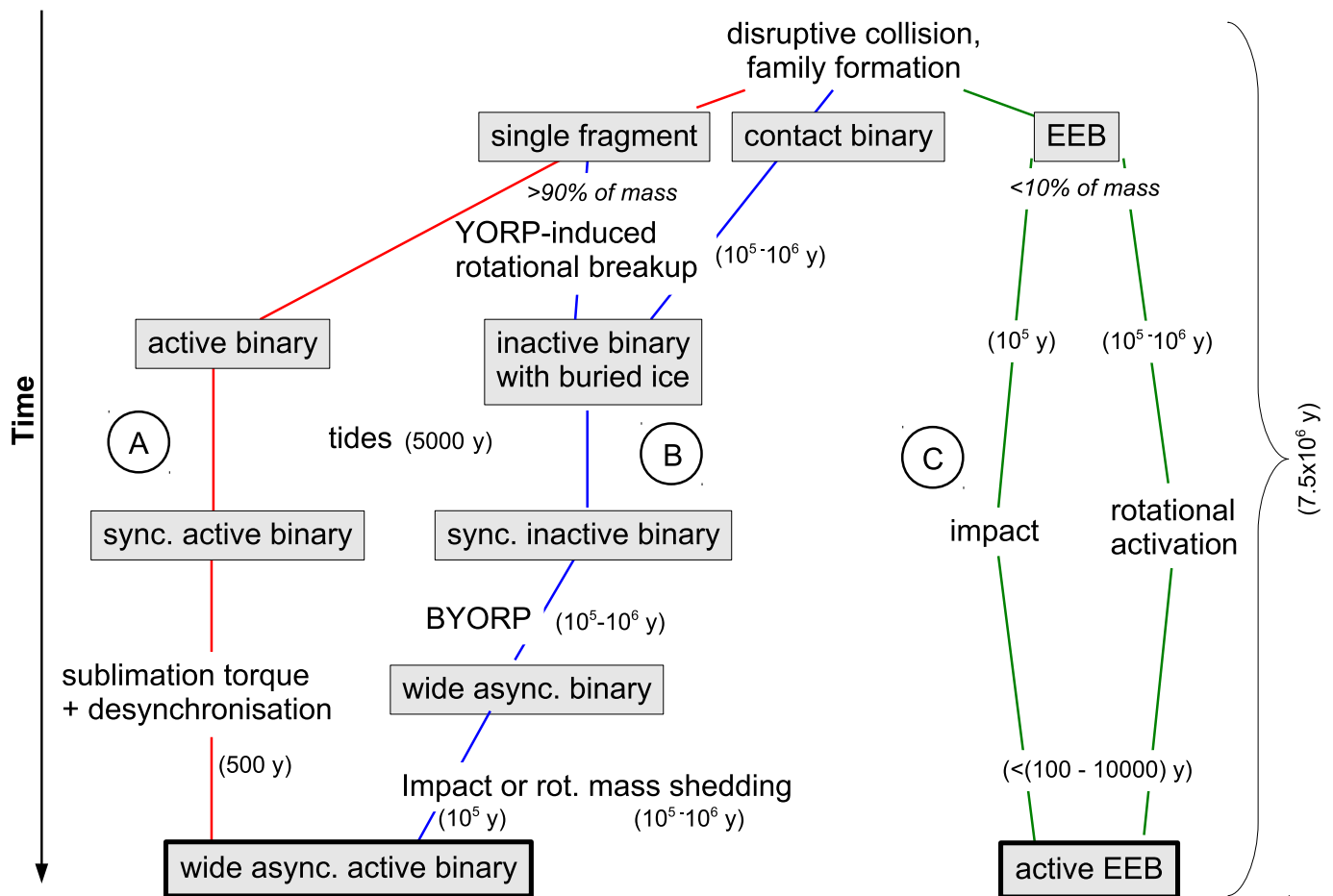
Extended Data Figure 3 | The central $8'' \times 4''$ of the coma and tail of 288P. The red and green lines correspond to the projected orbit and projected antisolar direction. Solid black lines show the loci of particles of fixed radiation pressure coefficient β (syndynes³⁶), with $\beta = 10^{-4}$, 10^{-3} , 10^{-2} and 10^{-1} in anticlockwise order. For a bulk density of $1,000 \text{ kg m}^{-3}$, this translates to particle sizes of 6 mm, $600 \mu\text{m}$, $60 \mu\text{m}$ and $6 \mu\text{m}$, respectively. The remaining lines (cyan, blue, and black-dashed) show synchrones³⁶, the loci of particles ejected at a given time. The colours correspond to the following ejection dates: solid cyan, 2016 July 19; dashed cyan, 20 days before and after that date; blue, 2016 September 29; dotted

black, 10 days before the observation; dashed black, 60 days before the observation. Up to September 09, the dust tail was oriented towards the direction where large dust grains (0.6–6 mm radius) ejected in July 2016 are expected. Beginning from September 20, a tail of 6–60- μm -sized particles developed in the projected antisolar direction and remained there up to the end of our observation campaign in January 2017. On those dates when the viewing geometry allowed us to distinguish between 6 and $60 \mu\text{m}$ (September 20 to October 26), the smaller-sized syndynes match the data better.



Extended Data Figure 4 | Dust production of 288P. The production rate was inferred from the coma brightness within a 400-km aperture for representative particle sizes of 6 μm and 60 μm . The production rates

represent lower limits (see Methods). The horizontal error bars represent the time that it takes dust to leave the 400-km aperture in which the dust brightness was measured. DOY, day of year.



Extended Data Figure 5 | Possible evolutionary paths of the 288P system. We assume that 288P is a fragment from a catastrophic collision 7.5×10^6 years ago¹⁵. Possible outcomes of this collision are (1) a single fragment or a contact binary, or (2) an EEB²¹. EEBs contain only a small fraction of the mass involved in a collision, while the bulk is in single fragments or contact binaries^{21,22}. An EEB could subsequently have been activated by either an impact of a 1-m-radius body, or by rotational mass shedding after YORP-acceleration (path C). The average time between such impacts is 10^5 years, whereas the YORP spin-up time is 10^5 to 10^6 years (ref. 18). The sublimation can last more than 5,000 years (ref. 28). If 288P evolved out of a single fragment or a contact binary, it could have split into a binary by rotational fission on a timescale of 10^5 – 10^6 years. Subsequently, the binary and spin periods must have tidally synchronized,

to enable binary YORP (BYORP) or sublimation torques to further expand the semimajor axis. The timescale for tidal synchronization of an equal-mass binary is 5,000 years (ref. 18), such that activity triggered upon splitting could have prevailed at the time of synchronization. In that case (path A), sublimation torques could have expanded the binary orbit to its present state on timescales of 500 years. If the system was not active at the time of synchronization (path B), the orbit expansion would have to be attributed to the binary YORP effect, which takes several orders of magnitude longer than sublimation torques. The activity would in this case have had to be triggered by an impact or rotational mass shedding following renewed YORP spin-up. The timescales for path B are longer than for path A but well within the age of the 288P family.

Extended Data Table 1 | Parameters of the HST observations

N	UT Date	DOY16	r_h [AU]	Δ [AU]	α [deg]	PA_{\odot} [deg]	PA_{-v} [deg]	ϵ [deg]	long [deg]	lat [deg]
1	2016-Aug-22	235.16	2.47	1.50	8.95	259.53	246.55	2.00	351.19	5.23
2	2016-Sep-01	245.67	2.46	1.46	4.54	275.56	246.88	2.17	349.36	-5.41
3	2016-Sep-09	253.50	2.45	1.45	2.25	330.82	247.19	2.24	347.81	-5.46
4	2016-Sep-20	264.16	2.45	1.46	5.33	42.83	247.64	2.22	345.69	-5.43
5	2016-Sep-29	273.33	2.44	1.49	9.23	54.45	248.00	2.12	344.13	-5.32
6	2016-Oct-26	300.83	2.44	1.69	18.65	63.63	248.43	1.45	342.31	-4.63
7	2016-Nov-04	309.60	2.44	1.78	20.61	64.73	248.31	1.18	342.83	-4.36
8	2016-Nov-13	318.42	2.44	1.88	22.06	65.50	248.08	0.90	343.87	-4.10
9	2016-Dec-14	349.50	2.44	2.27	23.74	66.83	246.86	0.01	351.00	-3.25
10	2016-Dec-26	361.40	2.45	2.42	23.29	67.12	246.40	-0.27	354.83	-2.97
11	2017-Jan-17	383.46	2.46	2.70	21.35	67.74	245.83	-0.66	2.92	-2.54
12	2017-Jan-30	396.23	2.47	2.85	19.70	68.26	245.74	-0.82	8.16	-2.31

N is the sequence number of the observation, r_h and Δ are the heliocentric and geocentric distances in astronomical units, α is the phase angle, PA_{\odot} and PA_{-v} are the position angles of the antisolar direction and of the projected negative orbital velocity vector, ϵ is the angle between the line of sight and the orbital plane of 288P, and long and lat are the observer-centred ecliptic longitude and latitude.

Extended Data Table 2 | Measured component separations

UT Date	S ["]	F_E [e ⁻ /s]	F_W [e ⁻ /s]
2016-Aug-22	0.0556	54.82	50.62
2016-Sep-01	0.0645	53.93	55.64
2016-Sep-09	0.0464		
2016-Sep-20	0.0213		
2016-Sep-29	0.0537	64.75	66.48
2016-Oct-26	0.0110		
2016-Nov-04	0.0000		
2016-Nov-13	0.0000		
2016-Dec-14	0.0253		
2016-Dec-26	0.0133		
2017-Jan-17	0.0095		
2017-Jan-30	0.0198		

For observations with separations S of more than two pixels ($0.05''$), the brightness of the individual components is also listed, where F_E and F_W refer to the eastern and western component, respectively. The values represent the total flux within an aperture of radius 1.5 pixels ($r_{\text{ap}} = 0.0375''$) centred as indicated by the circles in Fig. 1 and are not background-subtracted, owing to the unknown distribution of the dust. The point spread function of WFC3/UVIS at 600 nm is $0.067''^{35}$, such that even at the largest observed separation, the point spread functions of the two nuclei overlap. Each $0.0375''$ aperture encircles 90% of the flux from the central nucleus. The energy from the neighbouring nucleus is contained to 83–88% (for $0.054 < S < 0.065$) within a circle of radius $S - r_{\text{ap}}$ not overlapping with the aperture, and to 5% outside a circle of radius $S + r_{\text{ap}}$ also not overlapping. Assuming that not more than half of the remaining energy falls into the aperture, this would be 3.5–6% of the total energy from the neighbouring source. Disregarding the dust contribution, the similar flux measured in the two apertures therefore reflects a similar brightness of the two point sources.